Construction and Building Materials 416 (2024) 135228

Contents lists available at ScienceDirect

Construction and Building Materials

journal homepage: www.elsevier.com/locate/conbuildmat

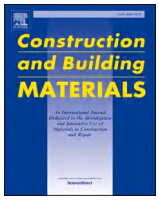

A combined weighted Voronoi tessellation and random field approach for modeling heterogeneous rocks with correlated grain structure

Yuexiang Lin [a,b], Zhengshou Lai [c,d], Jianjun Ma [c], Linchong Huang [a,c,*]

[a] School of Aeronautics and Astronautics Engineering, Shenzhen Campus of Sun Yat-sen University, Shenzhen 518107, China
[b] Department of Civil and Environmental Engineering, The Hong Kong Polytechnic University, Hong Kong, China
[c] School of Civil Engineering, Sun Yat-sen University, Zhuhai 519000, China
[d] School of Intelligent Systems Engineering, Shenzhen Campus of Sun Yat-sen University, Shenzhen 518107, China

ARTICLE INFO

Keywords:
Rock heterogeneity
Grain structure
Random field
Voronoi tessellation
Finite discrete element method

ABSTRACT

Construction rocks often exhibit a grain structure with spatially correlated grain formations, posing a challenge in quantifying and predicting their mechanical properties. Effectively quantifying and predicting the mechanical and fracturing behaviors of these construction materials is crucial for enhancing their exploitation and utilization efficiency. Misjudgments in this regard could lead to unacceptable fractures or even the collapse of rock formations during infrastructure constructions. This work proposes an approach that combines weighted centroidal Voronoi tessellation (WCVT) and random field (RF) to generate heterogeneous rocks with a correlated grain structure. WCVT is used to partition a rock domain into grains, and RF is adopted to control the grain sizes and the size correlation. With rock samples generated based on RF-WCVT, the finite discrete element method (FDEM) is introduced to simulate the mechanical behavior (typically the fracturing behavior) of heterogeneous rocks. The procedure for importing RF-WCVT-based rock samples into an FDEM model and inserting zero-thickness cohesive elements for modeling potential fractures is developed. Numerical examples are presented to demonstrate the effectiveness of RF-WCVT for generating heterogeneous rocks with a correlated grain structure, as well as the performance of FDEM in modeling the mechanical behavior of heterogeneous rocks. Effects of grain structure, in terms of scale of fluctuation and bedding orientation, on the mechanical behavior of rocks are analyzed.

1. Introduction

Construction rocks, such as columnar jointed rocks [40], porphyritic granite [66], crystalline rock [33], etc., are often featured with complex granular structures and may contain inherent defects, weak joint, and even open cracks at various scales, leading to significant complications and stochasticity in their mechanical behavior. Fig. 1(a) depicted several examples of rocks that exhibit a grain structure at various scales. These construction rocks are commonly employed in the production of various aggregates or synthetic rock slabs, serving as valuable materials in building construction and various infrastructure engineering projects. The microstructure of these construction rocks is featured with polyhedral-shaped grains [22]. The size, shape, orientation, and correlation of the grains vary significantly among these rocks, which proved to be the main sources of morphological heterogeneity in rocks [49,9]. Notably, the grain structure of theses rocks usually present both randomness and high spatial correlations[59,63,67]. These correlated and stochastic structures have a considerable influence on the microscopic and macroscopic mechanical behaviors of rocks. It thus brings many difficulties in the quantification and prediction of the mechanical properties and fracturing tendency of rocks.

Moreover, lots of widely used synthetic construction and building materials, such as cemented tailings backfill ([17,50]), asphalt mixture ([4,61])., phosphate mining backfill [46] as shown in Fig. 1(a), have been observed layered correlated grain structures[14]. This has created an urgent need for developing a systematic method to investigate mechanical characteristics of such natural or synthetic construction and building materials. Effective quantifying and prediction of the mechanical and fracturing behaviors of these construction materials is crucial for enhancing their exploiting and utilization efficiency. Furthermore, it can also improve the quality and safety of the projects that are constructed on or within these complicated rock formations, including dams [12], and minging tunnels [15,36,42], as misjudgments in this regard could lead to unacceptable fracutures or even collapse during the infrastructure constructions ([27,29,37,39,38,64]), as shown

* Correponding author at: School of Aeronautics and Astronautics Engineering, Shenzhen Campus of Sun Yat-sen University, Shenzhen 518107, China.
E-mail address: hlinch@mail.sysu.edu.cn (L. Huang).

https://doi.org/10.1016/j.conbuildmat.2024.135228
Received 31 July 2023; Received in revised form 30 December 2023; Accepted 26 January 2024
Available online 6 February 2024

Nomenclature

a	Acceleration
b	Unit body force
C_i	Voronoi cell
CVT	Centroidal Voronoi tessellation
D	Overall damage in the material
d	Eulerian distance between two points
E	Elastic modulus
G_{I}	Deformation creates fracture energies along normals
G_{II}	Deformation drives fracture energy along shears
k	Stiffness matrix
L	Lower part of Cholesky decomposition of covariance matrix $\boldsymbol{C}$
$N(\mu,\sigma)$	Gaussian distribution
P	Any point in the space of a domain
RF	Random field
S_i	Voronoi seed
S	Seed points
T_0	Constitutive thickness
U	Vector of independent random variables with the same length of Z
VT	Voronoi tessellation
WVT	Weighted Voronoi Tessellation
$WCVT$	Weighted Centroidal Voronoi Tessellation
W_i	The Weight assigned to seed i
x_{i}	A point in the space
μ	Mean
σ	Standard deviation
$\rho(\Delta x,\theta,\phi)$	Correlation function
Δx	Separation distance between locations
ϕ	Correlation orientation
$rot(\Delta x,\phi)$	Rotation function
Δx_x	Separation distance in x direction
Δx_y	Separation distance in y direction
θ_x	SOF along the x direction
θ_y	SOF along the y direction
ε	Strain
δ	Displacement
σ_n^0	Shearing strengths
τ_s^0	Tensile strengths
$\delta_m^{\max}$	Maximum effective displacement
δ_m^f	Effective displacement at complete failure
δ_m^0	Effective displacement at damage initiation
δ_n^0	Displacement at damage initiation for deformation develops along the shear directions
δ_s^0	Displacement at damage initiation for deformation develops along the normal directions
G_{I}	Fracture energies for deformation develops along the normal directions
G_{II}	Fracture energies for deformation develops along the shear directions
η	Material parameter
Z	A vector of random variables

in Fig. 1(b). To approach an accurate characterization of the mechanical behavior of the heterogeneous construction rocks, it is crucial to consider their spatially correlated and stochastic grain structures.

Physical model tests provide efficient and direct approaches to understand the influences of granular structures on the mechanical response of rock formations. With the help of advanced equipment and techniques, such as scanning electron microscope (SEM) [33,34], digital image processing (DIP) [40], acoustic emission (AE) [34], etc., many experimental studies have been conducted on natural rocks to investigate the relationships between the macroscopic mechanical properties and microscopic grain structures. Furthermore, some researchers adopted three-dimensional printing technique to create rock-like specimens with specified granular structures [45,57]. By conducting the uniaxial compression tests on these artificial specimens, the failure modes and mechanical behaviors have been extensively discussed. However, due to the heterogeneity of rocks, it is still difficult to approach an accurate characterization of the mechanical behavior (typically the fracturing behavior) of rocks through limited number of laboratory tests [66,67,9,8]. In addition, the microscopic parameters, such as the localized stress and strain, which is important to the understanding of the mechanical behavior of rocks, may not be directly measurable from laboratory physical tests [2]. Numerical simulation thus becomes an important complement to laboratory tests to investigate the effect of heterogeneous grain structure on the mechanical behavior of rocks. Rocks with granular structures are characterized by significant discontinuity, making it challenging to conduct effective analysis on these materials using continuous numerical approaches, such as the finite element method (FEM). To consider the discontinuity caused by granular structures, there are two groups of numerical methods that are widely adopted to model the mechanical behavior of rocks with granular structures, namely the discontinue-based methods and the combined continuum-discontinue methods. The discrete element method (DEM) has been one of the most widely used discontinuum-based methods [6,62]. DEM is usually integrated with the grain-based model (GBM) to model heterogeneous rocks [66]. In GBM, particles in a grain are bonded with each other where the bond behavior is characterized by bond models (e.g., parallel bond model [44]), and the inter-grain interactions is modeled by contact models such as the widely used smooth-joint model (SJM) [5,7]. The grain size effect on the mechanical behavior of rocks have been discussed in Zhou et al., [66], where simulation results indicate that the mechanical behavior of rocks could vary significantly with grain sizes. Although grain structure has been considered in these studies, the issue of unrealistically low peak strength is often identified [25]. It is because that most GBM-DEM models adopt spherical particles as basic elements, which may not well reflect the effect of shape irregularity and grain interlocking on the mechanical behavior [8,23,24].

As rocks with grain structures are featured with both continuum and discontinum characteristics, recently the coupled continuum-discontinuum methods have been increasingly employed to approach a more realistic prediction of the mechanical behavior of rocks. For instance, Liu et al. [34] and Wu et al. [54,55,56] developed a hybrid numerical approach known as the Voronoi element based-numerical manifold method (VE-NMM) to study the micro/macro-mechanical properties of crystalline rocks. This method allows fractures to propagate through mineral grains, thus avoiding mesh dependency issues. Another prevalent hybrid method is the finite-discrete element method (FDEM) ([32,47]). In FDEM, the deformation of rock grains is modeled by triangular elements, which are enhanced by joint elements and DEM algorithms to model the fracturing and contact behavior ([40,55,56,58,59]). By integrating with the Voronoi tessellation (VT) method for modeling the grain structure of rocks, the effects of the grain boundary density, thickness, and grain properties on the mechanical strength of rocks have been investigated [5,55,56,58].

Apart from choosing a suitable numerical method, replicating realistic grain structures of rocks is also critical to obtain accurate evaluations of their mechanical properties. With the help of software packages such as Neper, rocks with complex polycrystalline can be generated and

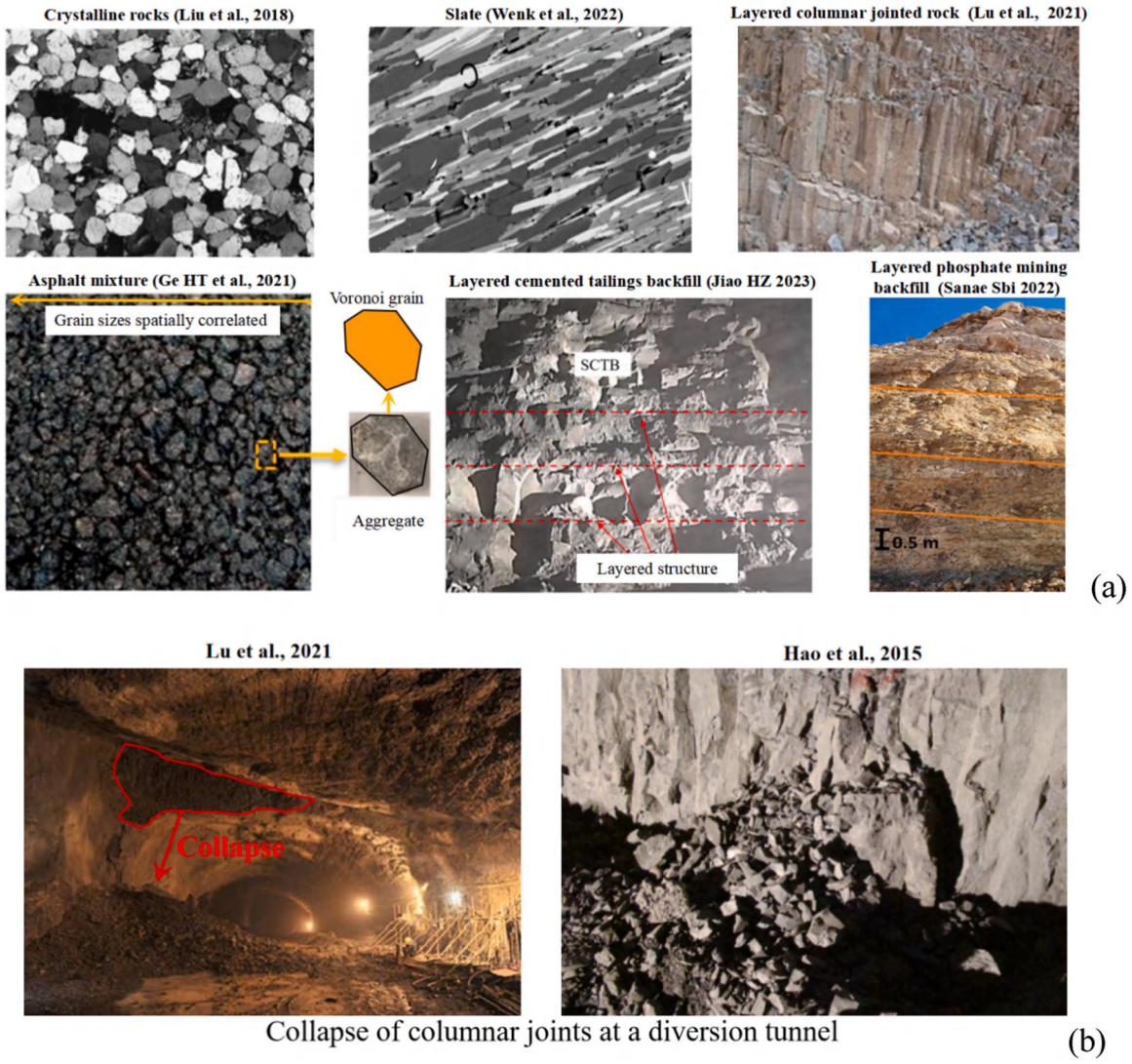

Fig. 1. Several examples of rocks that exhibit a grain structure (a) and engineering hazards in tunnel projects (b).

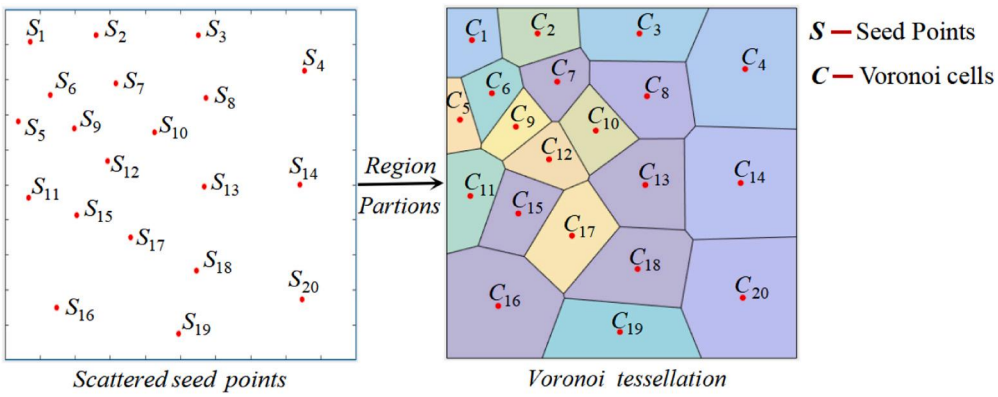

Fig. 2. Illustration of partitioning a domain into cells based on VT.

imported into various computational numerical methods for simulating their mechanical behavior[18]. However, the grains in a rock may exhibit various sizes that obey a certain distribution and spatial correlation (see Fig. 1). The fact of correlated grain structure in rocks cannot be well reproduced by the ordinary VT or centroidal VT (CVT) used in previous studies [9,10,11,29,63]. The correlation of grain structure could have significant impact on the mechanical and typically the fracturing responses of rocks [55,56]. To model a spatially varying and correlated field property in a reliable and efficient manner, the random field (RF) approach has been widely adopted[1,16]. RF has shown promising results in various applications, such as the simulation of cross-correlated soil properties for probabilistic stability analyses of

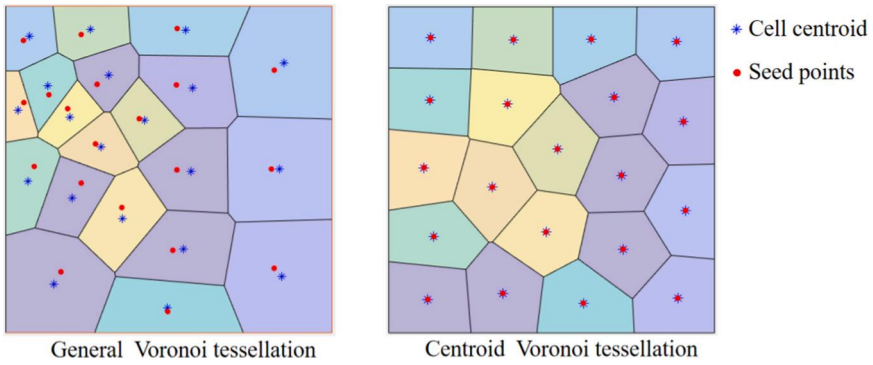

Fig. 3. Illustration of general VT and CVT.

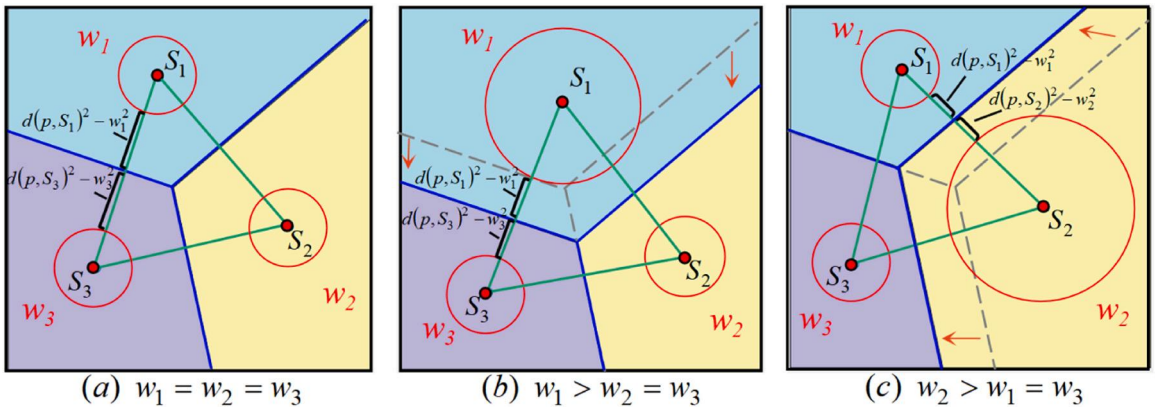

Fig. 4. Illustration of domain partitioning based on WVT.

slopes [13,35,20], and the areal mapping of soil compaction effectiveness with spatial correlations [19,26,30]. However, to the authors' best knowledge, no research has integrated the RF approach with VT to reproduce the micro-structure of rocks containing spatially correlated and stochastic grain cells, which may result in unsatisfactory predictions of mechanical properties in numerical analysis.

This work aims to develop an approach for generating rocks with correlated and stochastic grain structure and to investigate the effect of grain size correlation on the mechanical behavior of rocks. VT will be combined with RF to generate rocks with the grain sizes following a specific distribution and spatial correlation. The FDEM approach with a cohesive zone model will be introduced and validated to model rocks with a correlated grain structure. The effect of grain size correlation, in terms of scale of fluctuation (SOF) and bedding orientation, on the mechanical behavior of rocks will be investigated.

2. Generation of heterogeneous rocks with correlated grain structure

As mentioned above, rocks often present a grain structure with the grain sizes varying in space and following a spatial correlation. The combined RF and VT approach for generating heterogeneous rocks with correlated grain structure is presented in this section.

2.1. Weighted centroidal Voronoi tessellation (WCVT)

In general, a VT (also called a Voronoi diagram) is geometric partitioning technique that divides a space into regions based on the distances to a set of points. As illustrated in Fig. 2 in two-dimensions, a VT requires a set of distributed points (i.e., the red points in Fig. 2), which are called Voronoi seeds. The regions (i.e., C_i in Fig. 2) are called Voronoi cells, which are defined by points within specific distances to the Voronoi seeds. Each Voronoi seed S_i corresponds to a Voronoi cell C_i. The Voronoi cell C_i for seed S_i consists of all points that are closer to this seed than to any other, which can be mathematically expressed as

$$C_i = \{p \in \Omega | d(p,S_i) < d(p,S_j)\ \} \quad S_j \in S, j \neq i \tag{1}$$

where p represents any point in the space of a domain Ω, d represents the Eulerian distance between two points, S represents the set of all seed points.

Based on VT, a CVT is a special type of VT wherein the seed of a Voronoi cell is also the centroid of this cell. Comparing with a general VT, the cells of a CVT would be more equally sized and uniformly distributed in the space, as exemplified in Fig. 3. Nonetheless, there lacks a way to control the cell sizes in either VT or CVT. To address this issue, the weighted VT (WVT) is further utilized.

In WVT, each Voronoi seed is associated with a weight, and each Voronoi cell consist of all points with the following criterion:

$$C_i = \{p \in \Omega | dw(p,S_i,w_i) < dw(p,S_j w_j)\ \} \quad S_j \in S, j \neq i \tag{2}$$

where $dw(p,S_i,w_i) = d(p,S_i)^2 - w_i^2$, with w_i being the weight assigned to seed i. As illustrated in Fig. 4, a cell would have a larger area if its corresponding seed is specified with a larger weight, comparing with its neighboring seeds. Taking S_1 and S_2 for instance, the increase of w_1 and w_2 would force the Voronoi cells C_1 and C_2 to expand, such that Eq. (2) would be satisfied. Thus, the WVT provides a way to control the sizes of the cells by prescribing the weights of each seed. And, similar to the definition of CVT, a weighted centroidal Voronoi tessellation (WCVT) is the WVT with each Voronoi seed located at the centroid of each Voronoi cell.

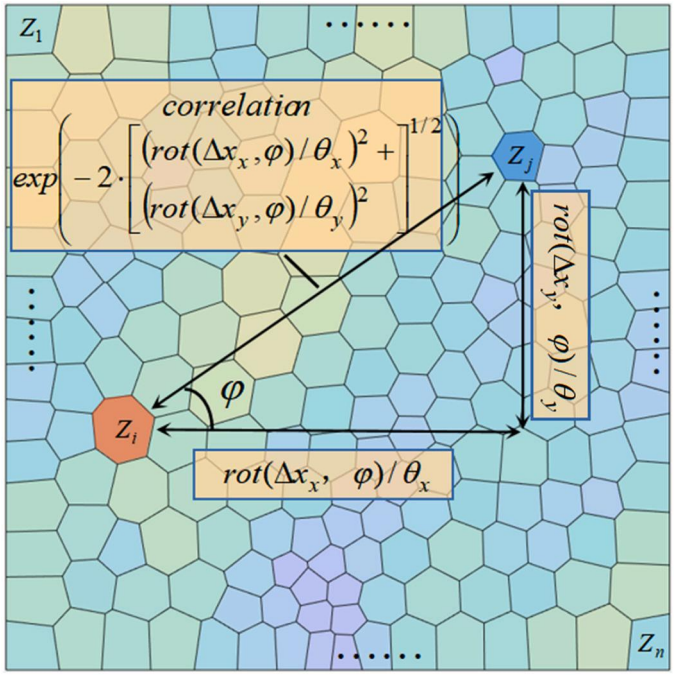

Fig. 5. Illustration of the correlation between the grain size at two locations.

2.2. Random field (RF) of grain sizes

Whereas the WCVT could be used to generate the grain structure of a rock, a key question that remains is how to determine the weight of each seed, so that the resultant grain sizes would present the desired spatial correlation. To address this question, the RF is utilized.

A RF is a variable defined on a n-dimensional Euclidean space Ω, where $\boldsymbol{x} \in \Omega$ represents a point in the space. Considering a set of n locations, a RF can be then quantified as a vector of random variables $\boldsymbol{Z}$, with $\boldsymbol{Z} = [\boldsymbol{Z}_1, \boldsymbol{Z}_2, ., \boldsymbol{Z}_n]$ representing the values of $\boldsymbol{Z(x_i)}$, where $i = 1, 2, .,$ n are the indexes the locations. In the case of a stationary RF with Gaussian distribution, the random variables $\boldsymbol{Z_i}$ would be obey distribution

$$Z_i = N(\mu, \sigma) \tag{3}$$

where $N(\mu, \sigma)$ represents the Gaussian distribution with mean μ and standard deviation σ.

In addition, the correlation between variables $\boldsymbol{Z_i}$ and $\boldsymbol{Z_j}$ can be described by a correlation function $\rho(\Delta \boldsymbol{x}, \theta, \phi)$, where the variable $\Delta \boldsymbol{x}$ represents the separation distance between location i and j, as shown in Fig. 5. For example, a single exponential function [21], as adopted in this work, is written as

$$\rho(\Delta x, \theta, \phi) = \exp\left(-2\cdot\left[\left(rot(\Delta x_x, \phi)/\theta_x\right)^2 + \left(rot(\Delta x_y, \phi)/\theta_y\right)^2\right]^{1/2}\right) \tag{4}$$

where ϕ represents correlation orientation, $rot(\Delta x_x, \phi)$ represents rotation function, Δx_x and Δx_y represents the separation distance in x and y direction respectively, θ_x and θ_y is the SOF along the x and y directions, respectively.

To sample the values of random variable $\boldsymbol{Z_i}$ in a field, the Cholesky decomposition approach [3] is adopted in this work due to its simplicity and efficiency. By using the Cholesky decomposition, the correlated random variables $\boldsymbol{Z_i}$ can be related to a set of independent random variables through

$$Z = LU \tag{5}$$

where U is a vector of independent random variables with the same length of $\boldsymbol{Z}$ and $\boldsymbol{L}$ is the lower part of Cholesky decomposition of

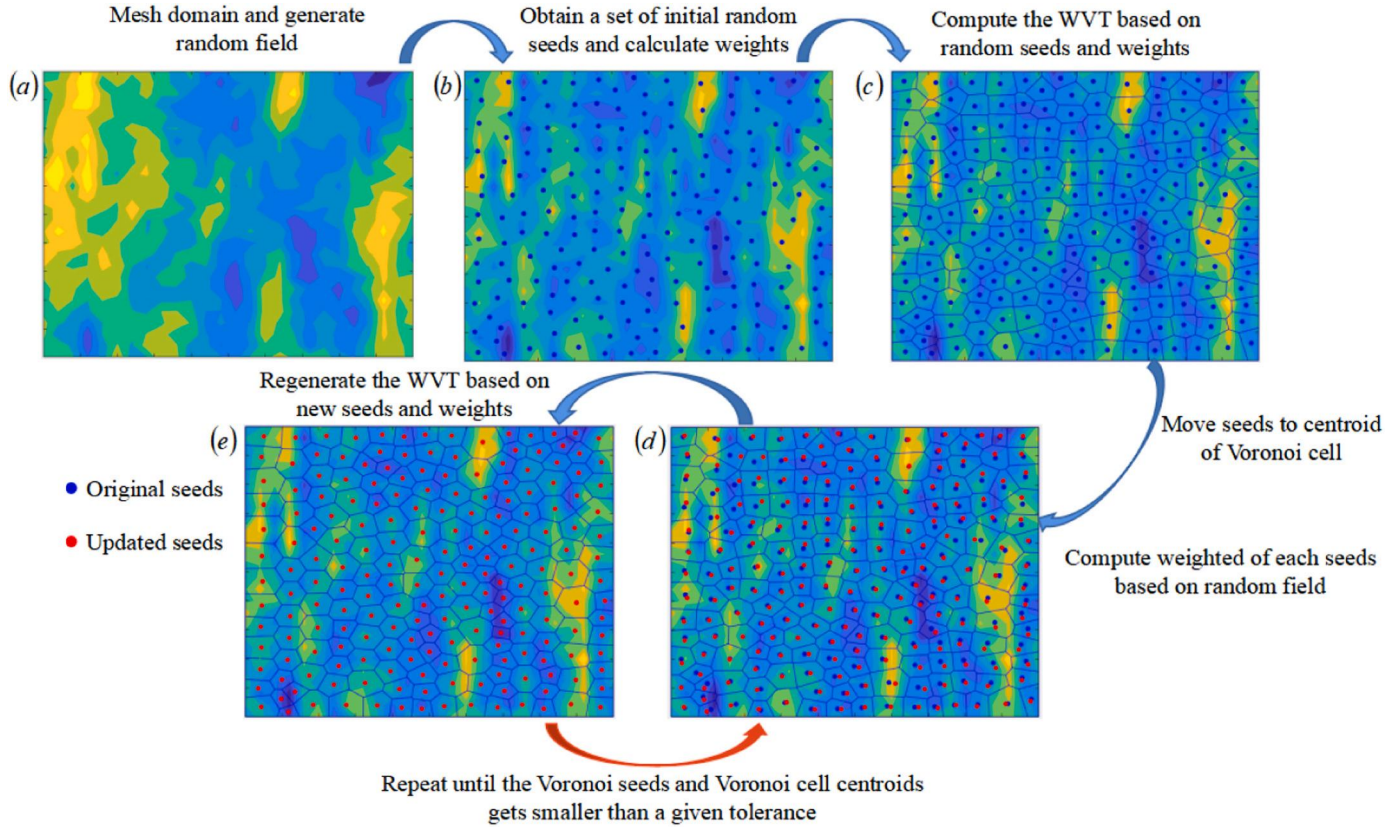

Fig. 6. Procedure of RF-WCVT for generating heterogeneous rock with correlated grain structure.

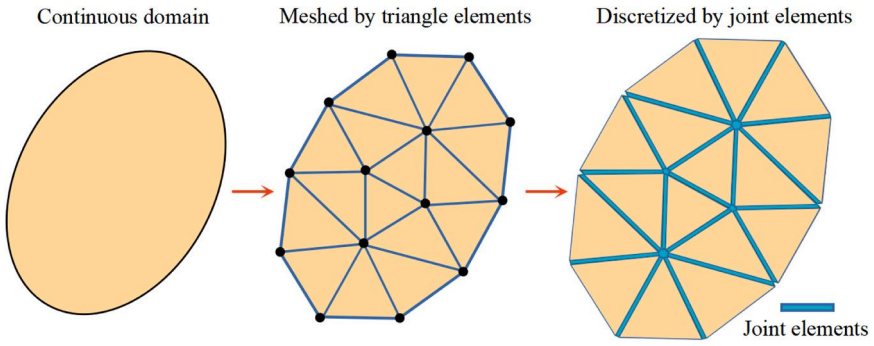

Fig. 7. The basic concept of FDEM.

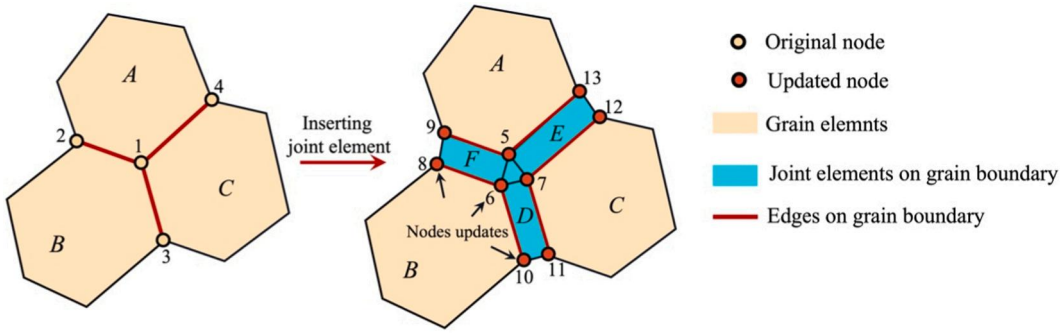

Fig. 8. Insertion method and structural characteristics of joint elements.

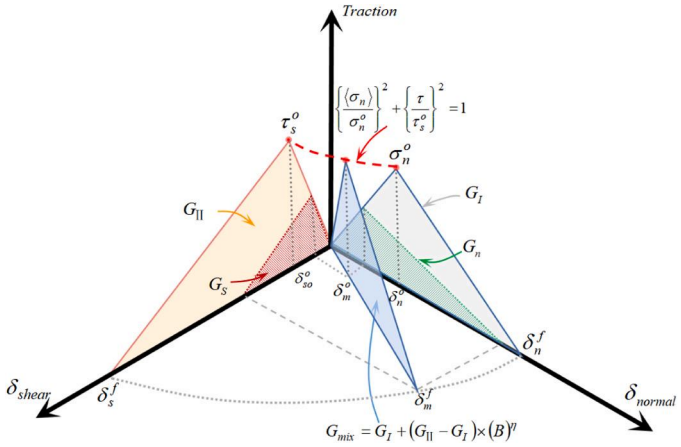

Fig. 9. Illustration of the mix mode of fracturing criterion for joint elements.

covariance matrix $\boldsymbol{C}$ satisfying $\boldsymbol{C}=\boldsymbol{L}\boldsymbol{L}^T$. The matrix $\boldsymbol{C}$ is n-order symmetric matrix which consists of ρ_{ij} calculated from Eq. (4). By combing Eqs. (3)–(5), a correlated random field with a specific orientation and correlation distance can be generated conveniently.

2.3. Generation procedure

With the formulation of WCVT and RF, the procedure of the combined RF and WCVT (RF-WCVT) to generate heterogeneous rocks with correlated grain structure is described as follows.

Table 1
The RF statistics of the grain sizes used in the RF-WCVT approach. The SOF is normalized by the mean grain size.

RF statistics of grain sizes	Specimen A	Specimen B	Specimen C
Mean (μ)	35.7 mm	29.4 mm	25.2 mm
Standard deviation (σ)	3.6 mm	4.5 mm	5.0 mm
SOF in the major principal axis (θ_x)	10	100	200
SOF in the minor principal axis (θ_y)	1	1	1
Bedding orientation (ϕ)	0°	45°	90°

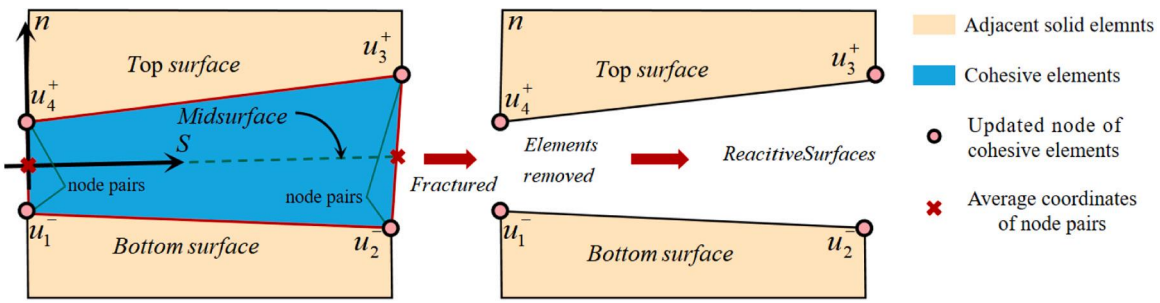

Fig. 10. Illustration of the definition of normal and shear directions of a joint element.

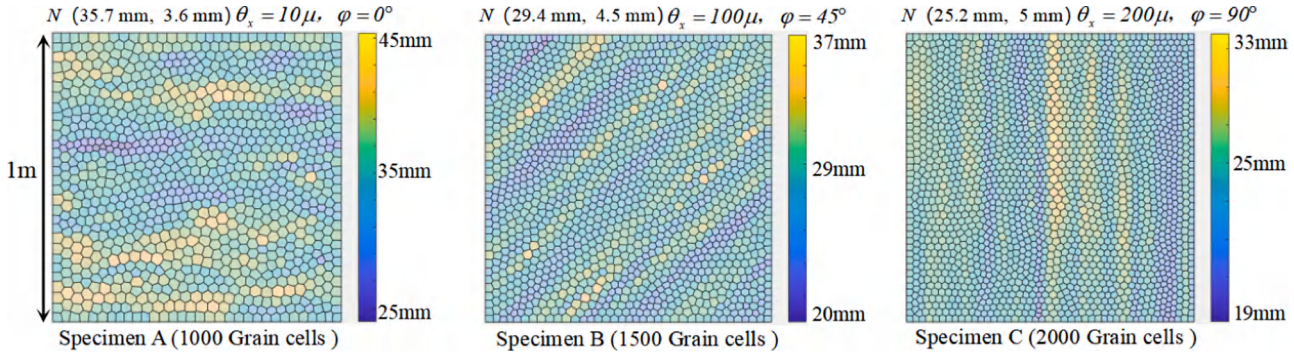

Fig. 11. Rock samples generated based on RF-WCVT with different grain structures. The color represents grain sizes.

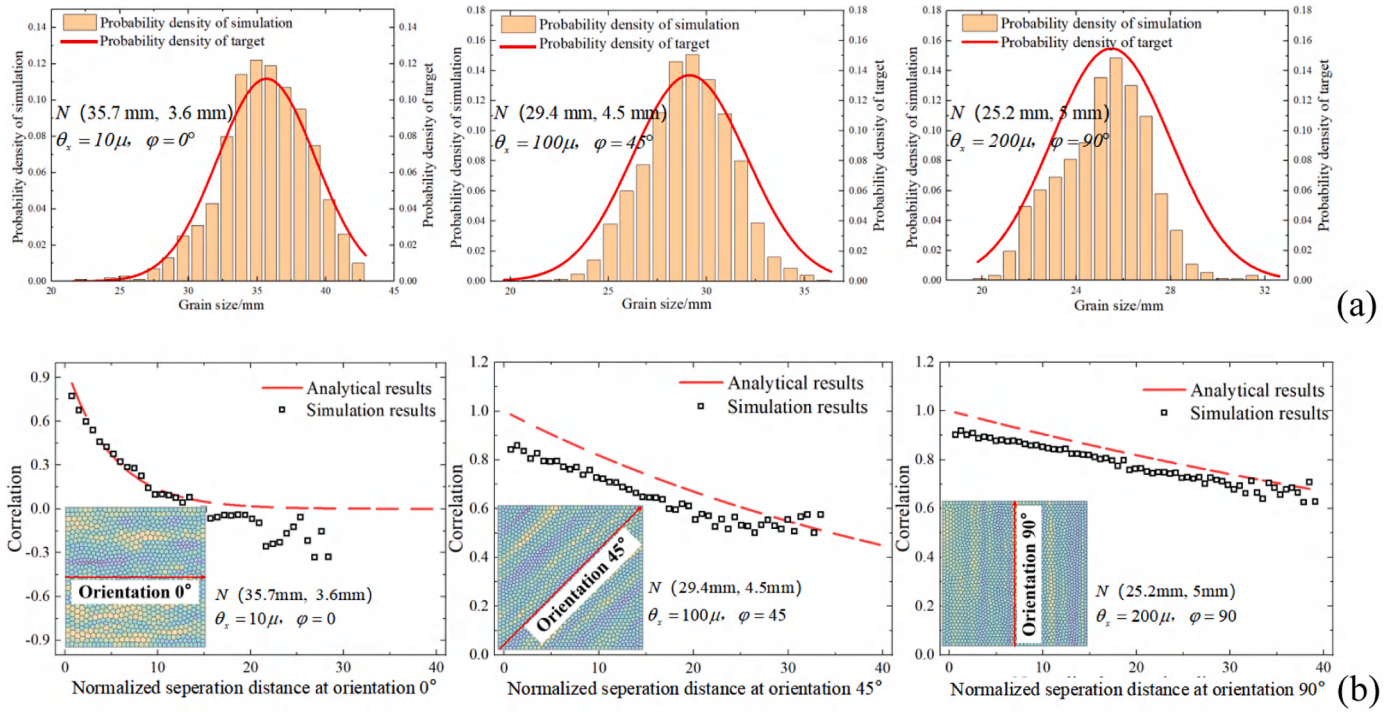

Fig. 12. Comparison of (a) grain size distribution and (b) grain size correlation between the RF-WCVT simulations and analytical calculations.

(1) Discretize a given domain into a set of mesh elements and obtain a RF of grain sizes at the centroids of the mesh elements using the Cholesky decomposition approach (i.e., Eq. (3)), as shown in Fig. 6(a).
(2) Estimate the number of grains required to fill the domain based on the given grain size distribution and domain size.
(3) Obtain the set of initial seeds, which could be sampled with random locations or extracted from a structural grid, as shown in Fig. 6(b).
(4) Compute the weight of each seed by interpolating the grain size at each seed from the RF of grain sizes obtained in Step (1).
(5) Compute the WVT based on the present seed locations and seed weights, where many commercial or open-source software tools, such as MATLAB and Voro+ + (http://math.lbl.gov/voro++/), can be adopted for such a task. The result of this step is illustrated in Fig. 6(c).
(6) Compute the centroid of each Voronoi cell and move the corresponding seed to the centroid of the cells, as illustrated in Fig. 6 (d).
(7) Repeat Steps (4)-(6) until the mean of the distances between the Voronoi seeds and Voronoi cell centroids gets smaller than a given tolerance, or it reaches the maximum number of iterations.

The proposed RF-WCVT can generate grain structures with both grain sizes and spatial correlation quantitatively controlled. This method can be extended to many numerical methods, such as the Discontinuous Deformation Analysis (DDA) [39], Discontinuous Element Method (DEM) (Lai et al., 2023), and Distinct Lattice Spring Model (DLSM) [39]. However, it is important to note that when applying these discontinuous methods, additional algorithms must be incorporated to fill the grain cells with basic elements. The filling process inevitably introduces unexpected porosity, potentially influencing the mechanical strengths and failure patterns during modeling. This aspect should be carefully considered and addressed in the parameter calibration process. In contrast, the FDEM method is characterized by both continuity and discontinuity, effectively avoiding the problem introduced by the filling process.

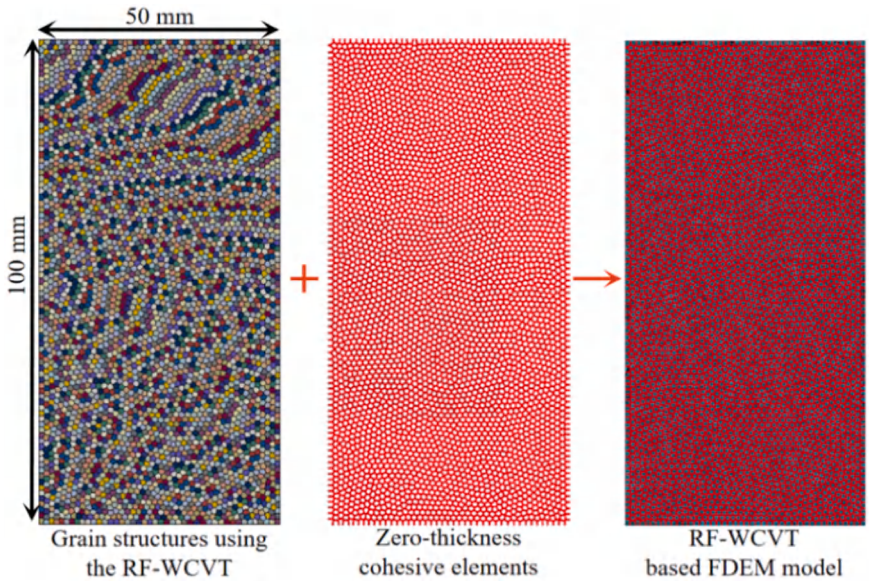

Fig. 13. WCVT-based FDEM model for the example crystalline rocks.

Table 2
FDEM material properties of the crystalline rock.

Mechanical Parameters	Values
Density (kg/m^3)	2590
Young's Modulus (GPa)	40.3
Poisson's ratio	0.314
Normal stiffness (GPa)	18.0
Shear stiffness (GPa)	3.6
Friction angle (°)	33.0
Cohesion (MPa)	16.0
Tensile strength (MPa)	5.5
Mode-I fracture energy (N/m)	26.1
Mode-II fracture energy (N/m)	104.4

3. RF-WCVT-based FDEM for modeling heterogeneous rocks

FDEM is an effective numerical tool to model heterogeneous materials with both continuum and discontinuum characteristics [55,58]. By adopting the joint elements to trace fracturing behaviors, the initiation, intersection, and propagation of fractures can be well captured by FDEM ([31,28,49,58]). In this section, the formulation of FDEM for modeling heterogeneous rocks is briefly described for the sake of completeness. The integration of correlated rock grain structure generated based on the proposed RF-WCVT approach into an FDEM model will be also presented.

3.1. Formulation of FDEM

In this work, FDEM is employed to solve the balance of momentum equation written as

$$\nabla \bullet \boldsymbol{\sigma} + \rho \boldsymbol{b} = \rho \boldsymbol{a} \tag{6}$$

where $\boldsymbol{\sigma}$ is the stress, ρ is the density, $\boldsymbol{b}$ is the unit body force, and $\boldsymbol{a}$ is the acceleration. FDEM usually involves two types of elements, namely the conventional solid elements for capturing the deformation of material, and the joint elements for modeling fracturing behavior. Fig. 7 illustrates the basic concept of FDEM. For a two-dimensional continuum domain, it is first discretized into conventional mesh elements. Then, joint elements are inserted on the edges of the prior elements to obtain the final FDEM model. The joint elements are initially assigned zero thickness to ensure that the geometric continuity of the model is maintained. The initiation and propagation of fractures are thereby modeled by the deformation of the joint elements. In addition, once a joint element fail, the interactions among the connected triangular elements will be approached by contact mechanics.

To integrate RF-WCVT into the FDEM approach, the continuum domain is first partitioned using RF-WCVT, as shown in Fig. 8. Rather than inserting the joint elements ubiquitously, the zero-thickness joint elements are only adopted on the boundaries of the grains. It is because that the grain boundaries are considered to be much more vulnerable than the inner of rock grains and have been proved to be the main fracturing paths of rocks (Liu et al., 2018a). The insertion of joint elements into the grain boundaries is implemented by first replicating and renumbering element nodes on the boundary edges, (i.e., nodes 1–4 in Fig. 8) and then creating joint elements using the newly created nodes. For example, node 4 is replaced by the nodes 5–7 that share the same coordinates with node 4. The procedure is applied to all the nodes on the grain edges. Then, joint element E can be created from nodes 5–7-12–13. These inserted joint elements initially have zero initial thickness but will evolve in thickness during the fracturing process. It should also be note that the generation of numerous boundary elements in the RF-WCVT-based FDEM may lead to a lack of computational efficiency, which constitutes a primary drawback of the proposed method. However, this drawback has been significantly alleviated in 2D modeling due to the remarkable advances in computer chips and parallel computing strategies.

3.2. Constitutive models of joint elements

In the present FDEM model, the elastic constitutive model is adopted for the regular elements for simplicity. The bi-linear model with a mix fracture criterion is adopted for the joint elements. The classical Coulomb friction model is widely accepted due to its clarity and ease of implementation, and many previous studies have employed it in the FDEM modeling process as a common treatment of element contact post-failure [55,65], which has justify the adoption of the classical Coulomb friction model. Thus, in this study, the classical Coulomb friction model is adopted to evaluate the contact dynamics between regular elements after joint elements fail. In addition, the primary focus of this study is on the mechanical strengths and fracturing characteristics of rocks with spatially correlated grain structures. Throughout most of this process, the rock specimen has not experienced complete failure. Consequently, the adoption of the classical Coulomb friction model has limited impact

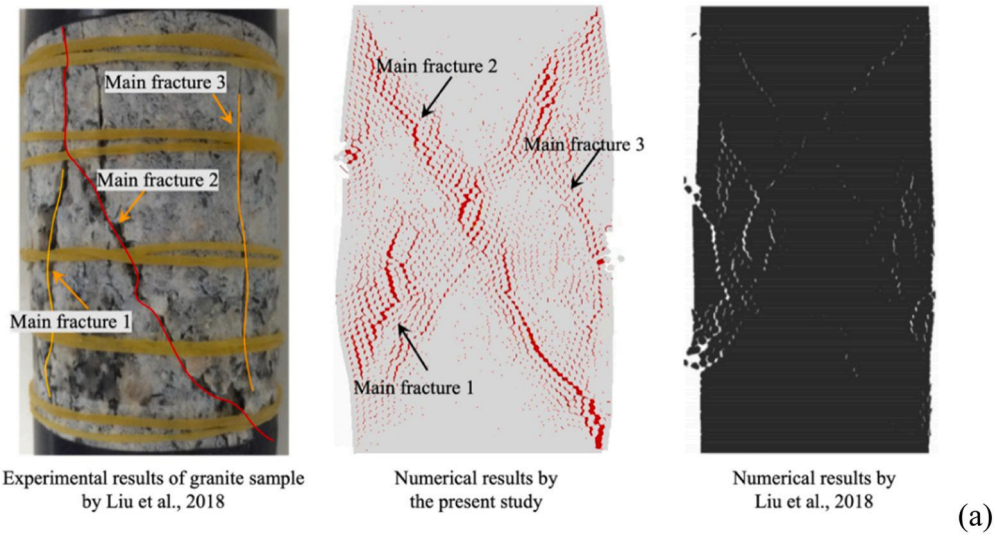

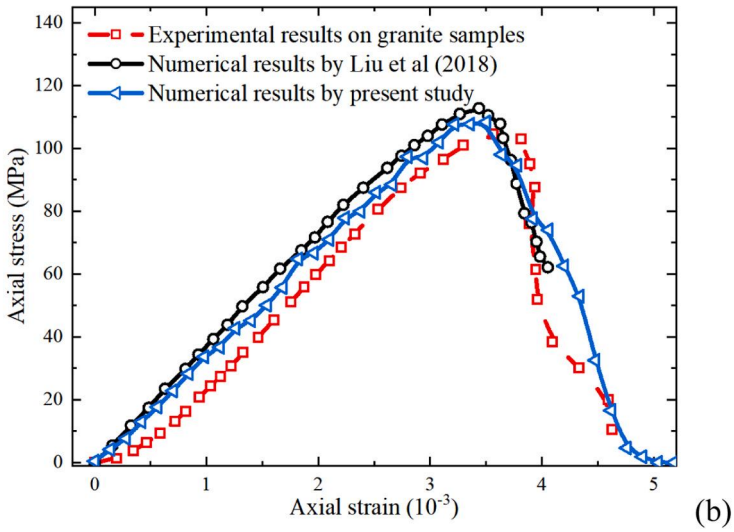

Fig. 14. The fracture pattern (a) and stress-strain behavior (b) of the example crystalline rock based on WCVT and FDEM, comparing with the results of laboratory experiments and VE-NMM in [34].

on the simulation results presented in this study. For the bi-linear model of joint elements, the stress-strain behavior is governed as

$$\sigma = \begin{Bmatrix} \sigma_n \\ \sigma_s \end{Bmatrix} = \begin{Bmatrix} E_{nn}E_{tn} \\ E_{nt}E_{tt} \end{Bmatrix} \begin{Bmatrix} \varepsilon_n \\ \varepsilon_s \end{Bmatrix} = \frac{1}{T_0} \begin{Bmatrix} E_{nn}E_{sn} \\ E_{ns}E_{ss} \end{Bmatrix} \begin{Bmatrix} \delta_n \\ \delta_s \end{Bmatrix} = \begin{Bmatrix} k_{nn}k_{sn} \\ k_{ns}k_{ss} \end{Bmatrix} \begin{Bmatrix} \delta_n \\ \delta_s \end{Bmatrix} \tag{7}$$

where σ represents traction, ε represents strain, δ represents displacement, E and k are elastic modulus and stiffness matrix, respectively, T_0 represents the constitutive thickness, and n and s indicate the normal and shear directions, respectively.

The details of the mix mode fracture criterion are presented in Fig. 9. Previous research has shown that a fracture may appear even when the traction has not reached stress criterion along the normal or shear directions [48]. For the mix mode of fracture criterion, damage is assumed to initiate when the quadratic nominal stress criterion is reached

$$\left\{\frac{\langle \sigma_n \rangle}{\sigma_n^o}\right\}^2 + \left\{\frac{\tau}{\tau_s^o}\right\}^2 = 1 \tag{8}$$

where σ_n^o and τ_s^o represent the shearing and tensile strengths, respectively. A scalar damage variable D is introduced to represent the overall damage in the material. The damage D monotonically evolves from 0 to 1, which is calculated by

$$D = \frac{\delta_m^f\left(\delta_m^{\max} - \delta_m^o\right)}{\delta_m^{\max}\left(\delta_m^f - \delta_m^o\right)} \tag{9}$$

where $\delta_m^{\max}$ refers to the maximum effective displacement attained during the loading history. Note that the effective displacement is obtained by $\delta_m = \sqrt{\delta_n^2 + \delta_s^2}$. δ_m^f represents the effective displacement at complete failure, δ_m^o represents the effective displacement at damage initiation. The δ_m^f and δ_m^o are calculated following the Benzeggagh-Kenane (BK) fracture criterion [48]:

$$\begin{cases} \delta_m^f = 2 \times \left[G_I + (G_{II} - G_I) \times B^\eta\right]/k_m \\ \delta_m^o = \sqrt{\left(\delta_n^o\right)^2 + \left[\left(\delta_s^o\right)^2 - \left(\delta_n^o\right)^2\right] \times B^\eta} \end{cases} \tag{10}$$

where δ_n^o and δ_s^o represent the displacement at damage initiation for deformation develops along the normal and shear directions, respectively; k_m is the stiffness calculated by $k_m = k_n(1-B) + k_s B$, where $B = G_I/(G_{II}+G_I)$, with G_I and G_{II} being the fracture energies for deformation develops along the normal and shear directions, respectively; η is a

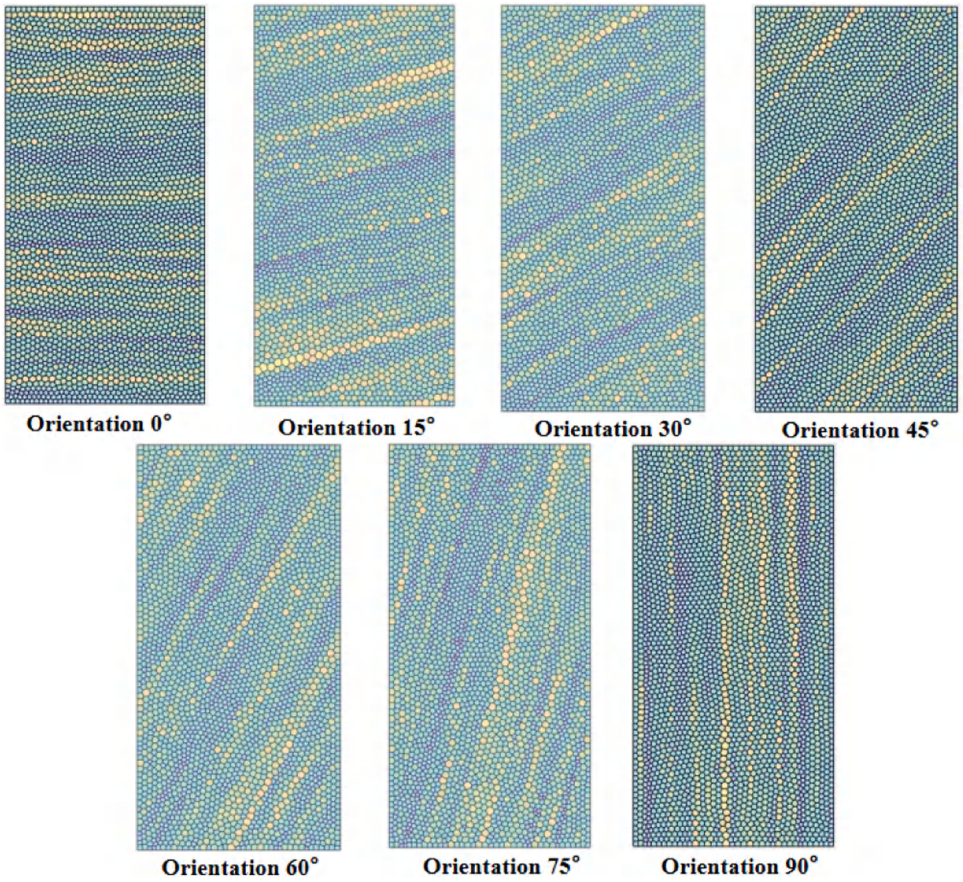

Fig. 15. Rock samples generated based on RF-SCVT with a variety of different grain bedding orientations.

material parameter.

Upon further loading, the stress components of the traction-separation model are affected by the damage according to

$$\begin{Bmatrix} \sigma_n \\ \sigma_s \end{Bmatrix} = (1-D)\cdot\begin{Bmatrix} k_{nn}k_{sn} \\ k_{ns}k_{ss} \end{Bmatrix}\begin{Bmatrix} \delta_n \\ \delta_s \end{Bmatrix} \tag{11}$$

To adopt bi-linear model and mix mode of fracture criterion in numerical modeling, the definition of normal and shear directions is quite critical, since the mechanical behavior of joint elements in the normal and shear directions is generally different. The following is a brief description of the strategy used to determine the normal and shear directions in joint elements. In Fig. 10, two solid elements are connected by a cohesive element, which consists of top and bottom surfaces that are determined from the element connectivity by default. To calculate the normal and shear directions of the cohesive elements, a midsurface is first created by averaging the coordinates of the node pairs (i.e., u_1, u_4 and u_2,u_3), as illustrated in Fig. 10. Next, the shear direction (i.e., *s*) is determined from the midsurface, while the normal direction (i.e., *n*) is obtained by the cross product of the out-of-plane and shear directions. Therefore, the normal opening and tangential slippage in the cohesive element can be expressed as

$$\begin{cases} \delta_n = \delta\cdot n \\ \delta_s = \delta\cdot s \end{cases} \tag{12}$$

where δ represents the displacement of node pairs, as $\delta = u_i^{+} - u_j^{+}$.

4. Numerical examples

This section presents several numerical examples to demonstrate the performance of the proposed RF-WCVT approach for generating rocks with correlated structure and the FDEM approach for simulating heterogeneous rocks. The effect of grain correlation on the mechanical behavior (typically the fracturing behavior) of rocks is investigated.

4.1. Results of RF-WCVT

The proposed RF-WCVT enables the generation of rocks with correlated grain structures. In this section, examples of generated rocks with different grain structures will be presented. The statistics of the grain sizes in a rock will be analyzed to investigate the effectiveness of RF-WCVT. As an example, a square domain with dimension of 1.0 m is considered. Rocks of different grain statistics (i.e., mean grain size, size deviation, SOF, and bedding orientation) are generated in this domain. The grain statistics are summarized in Table 1, and the corresponding rock samples are presented in Fig. 11. All generated rock samples exhibit clear layering profiles, with inclination angles close to the specified bedding orientation. The layering profile becomes more pronounced with increasing SOFs in the major and minor principal axes.

As a quantitative investigation, the statistics and spatial correlation of the grain sizes of these rock samples are evaluated, and the results are presented in Fig. 12. In Fig. 12, a square domain with dimensions of 1.0 m is utilized. To assess the efficiency of the proposed RF-WCVT, this square domain is filled with 1000, 1500, and 2000 grain cells, each corresponding to grain mean values of 35.7 mm, 29.4 mm, and 25.2 mm, as illustrated in Fig. 12(a). The variances are set at 0.1, 0.15, and 0.2 times the mean values, corresponding to 3.6 mm, 4.5 mm, and 5 mm in Fig. 12(a)., respectively. As expected, the generated grain sizes in Fig. 12(a) exhibit a Gaussian distribution, with the mean and standard deviation close to the target values listed in Table 1. In Fig. 12(b), the evolution characteristics of the correlation between two locations against location distances for the three different cases are illustrated.

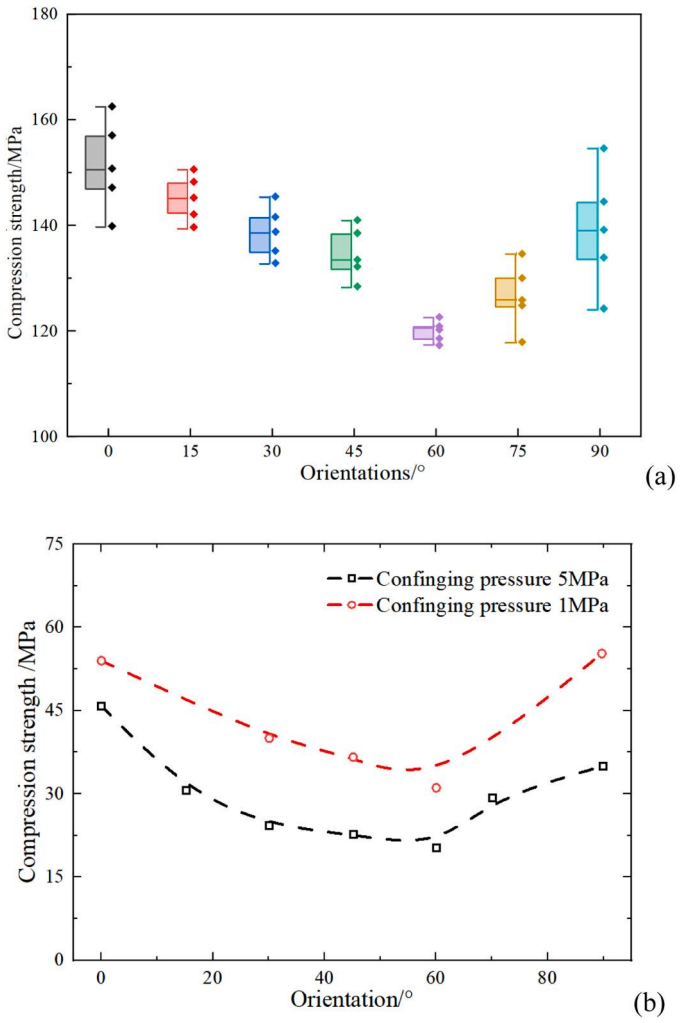

Fig. 16. (a) Box plot of the evolution of compression strengths with increasing grain bedding orientations. In each box, the central mark indicates the median, and the bottom and top edges of the box indicate the 25th and 75th percentiles, respectively. The whiskers are extended to the most extreme data points. The specific data of compression strengths are plotted individually on the right of the boxes. (b) Experimental data of bedding rocks (adapted from Niandou et al.).

Each point in the simulation results presented in Fig. 12(b) represents the mean size correlation of all pairs of grain cells that share the same distance. It is observed that both simulation and analytical results show a noticeable decrease in correlation with increasing location distances. Upon comparing the descending trends among the three figures in Fig. 12(b), it is evident that the decreasing trends become much gentler with the increase of SOF, according to both simulation and analytical results. The simulation results align well with the analytical results given by Eq. (4) in all cases, indicating that the spatial correlation between the grain sizes at different locations can be effectively regulated by adjusting the SOF in the proposed RF-WCVT method.

4.2. Validation of the RF-WCVT-based FDEM

To validate the RF-WCVT-based FDEM for modeling rocks, the experimental and numerical tests on crystalline rocks previously conducted by Liu and Wu (2018a) are employed as a comparison. Liu et al. [34] have developed the VE-NMM to simulate the mechanical and fracturing behavior of crystalline rocks under uniaxial compression test. Nonetheless, the VE-NMM has not considered the correlation structure of the grains in a rock. Similar to Liu et al. [34], a rock sample with mean grain size 1.25 mm, standard deviation 0.01 mm, and SOF of 1.25 mm (i.e., equivalent to the situation of no correlation) is generated based on RF-WCVT, as shown in Fig. 13. With this rock sample, the FDEM model is then created based on the procedure described in Section 3.1. Through this approach, the mechanical and fracturing behaviors are primarily influenced by the grain structures. The phenomenon of mesh dependence has a limited impact on the mechanical and fracturing responses in the proposed method. The optimal mesh size for the FDEM follows the recommended value provided by Liu et al. [34]. Table 2 presents the material properties used in the FDEM model, which were obtained from numerical tests conducted by Liu et al. [34]. The uniaxial compression test was conducted by imposing a deformation-driven loading velocity of 2.5 mm/s on the top boundary. Upon failure, the rock displayed a prominent shearing band, represented by the primary fractures 1 and 2, as marked in Fig. 14(a). This observation was consistent with the findings of the laboratory experiment. The axial stress-strain profile is presented in Fig. 14(b), exhibiting a good match with that of laboratory experiment, as well as the VE-NMM simulation reported in Liu et al. [34].

The VE-NMM reported by Liu et al. [34]. does not focus on the detailed characteristics of the Voronoi structures, utilizing a unified grain size for the Voronoi tesselation in numerical analysis. In contrast, the proposed RF-WCVT is designed to consider both grain spatial correlation and size distribution, offering adaptability to diverse scenarios with various requirements. To the best of the authors' knowledge, few existing methods can generate Voronoi grain structures with both grain correlation and size distribution being quantitatively controlled. It is essential to note that the numerical approach adopted in this method, i.e., FDEM, differs significantly from the NMM reported by Liu et al. The NMM by Liu et al. is also acknowledged as a functional and powerful hybrid numerical approach. Additionally, the proposed RF-WCVT can be embedded in the NMM to extend its application range, highlighting the value of the presented study.

4.3. Effect of grain size correlation on mechanical behavior of rocks

To gain insights into the effect of grain size correlation on the mechanical behavior of rocks, rock samples with different RF statistics are generated based on RF-WCVT and cast into FDEM for confined compression tests. In particular, the cases of different SOFs and bedding orientations are considered. A high SOF indicates that the grain sizes of two cells are likely to be close, even when a large distance separates them, resulting in pronounced layered structures. The bedding orientation represents the inclination angle of the layering profile.

4.3.1. Effect of grain bedding orientation

For the case of different grain bedding orientations, example rock samples of height 100 mm and width 50 mm are shown in Fig. 15. For all the rock samples, the mean grain size is kept the same as 1.25 mm and the standard deviation is 0.25 mm. The SOF is 100 times of the mean grain size. For the FDEM-based confined compression tests, the material properties are kept the same as those listed in Table 1. The loading velocity is taken as 2.5 mm/s and the confined compression is 1.0 MPa. For each set of RF statistics, five trials are performed to account for the effect of randomness.

The results of compression strength with increasing bedding orientations are plotted in Fig. 16. Herein, the compression strength is taken as the maximum axial stress during the confined compression test. The middle line for each box represents the mean of the scattered points. Since the specimens are randomly generated with controlled grain correlation and size statistics, the micro-structure of specimens varies. The insertion of zero-thickness boundary elements following these generated micro-structures can influence the complicated fracturing behaviors, leading to variance in compression strengths. However, a clear V-shaped evolution trend of the compression strength with increasing bedding orientation is observed, as shown in Fig. 16, indicating that the observed

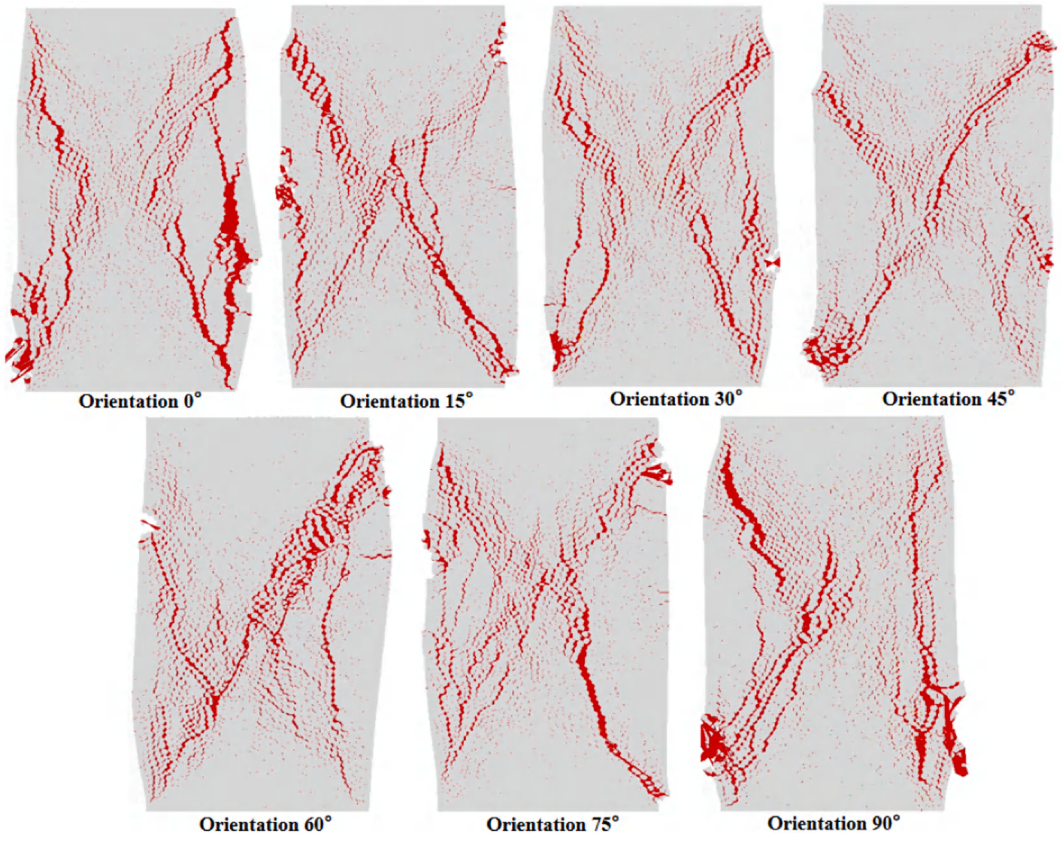

Fig. 17. Fracturing patterns of the rocks with various grain bedding orientations.

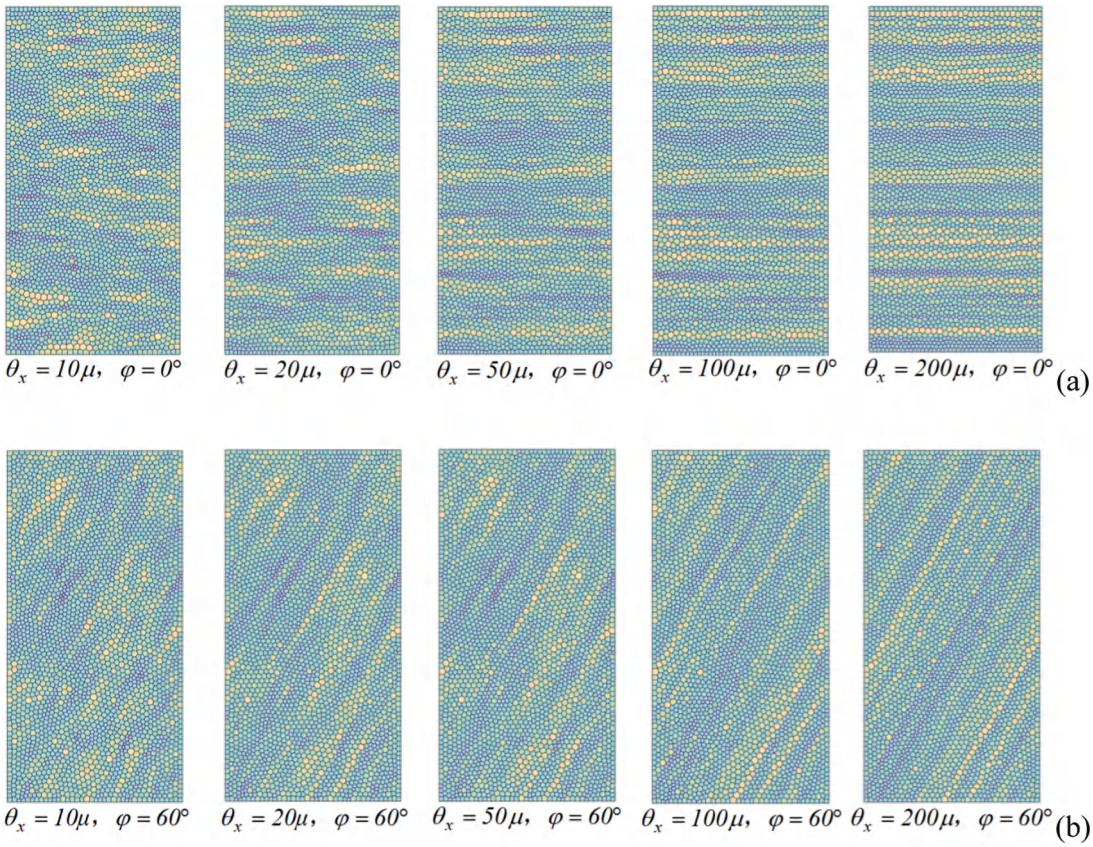

Fig. 18. Rock samples generated based on RF-WCVT with a variety of different SOFs: (a) bedding orientation 0° and (b) bedding orientation 60°.

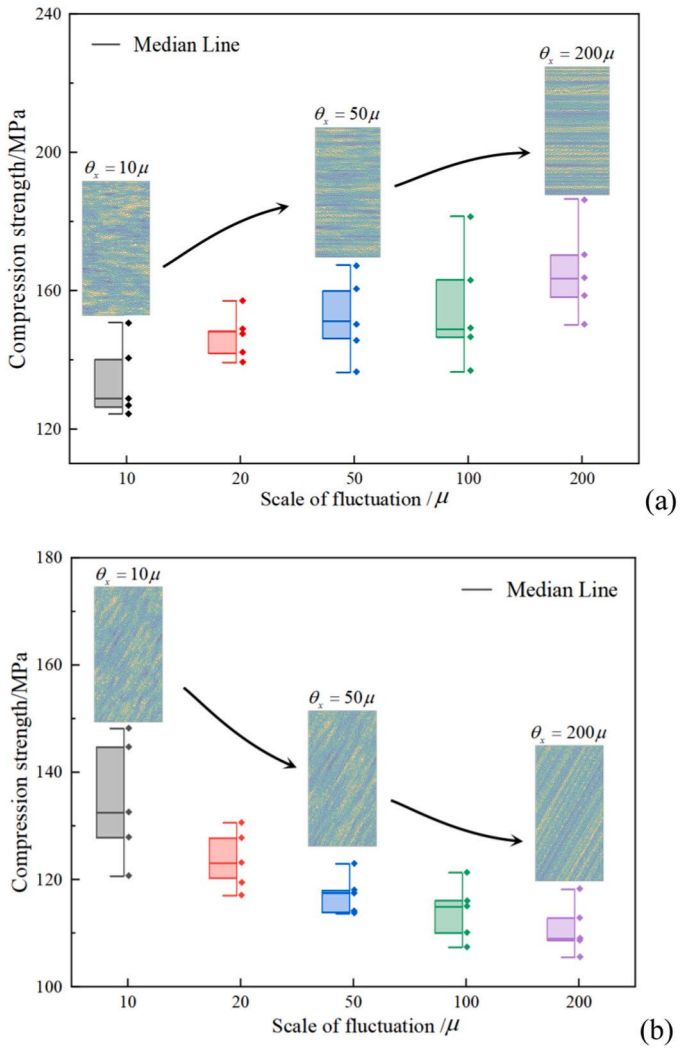

Fig. 19. Evolution of the compression strength with increasing SOF: (a) bedding orientation 0° and (b) bedding orientation 60°.

dispersion has limited impact on the evolution law of compression strength. The compression strength decreases with increasing bedding orientation when the orientation is less than approximately 60° but increases when the orientation exceeds 60°. In general, the compression strength of specimen with orientation 90° is smaller than that with an orientation of 0°. Such a phenomenon has also been observed in the experimental tests of bedding shale by Niandou et al. [43] and Yao et al. [60]. The experimental data has been presented in Fig. 16(b). As observed, the results from our proposed numerical approach align with experimental findings. This alignment provides another perspective, indicating that the presented RF-WCVT-based FDEM approach serves as an effective modeling tool for revealing and predicting the mechanical and fracturing characteristics of rocks with spatially correlated grain structures. Concerning the 'V' shape evolution laws of compression strength against orientation, a possible explanation could be provided by examining the failure modes of the rocks, as depicted in Fig. 17. For the cases of bedding orientation less than 30°, a X-shaped fracturing pattern accompanied by smeared cracks is observed in each specimen. However, the length and path of fractures decrease significantly with increasing orientation. For the cases of 45° and 60°, a clear shearing band can be observed, since the principal stress directions become close or even parallel to the grain bedding orientations. The failure patterns suggest that the layering profile of the rock grains would provide a favorable path for fractures to propagate. Consequently, fractures concentrate on the shearing band and develop rapidly, leading to a smaller fracturing area and lower compression strength. As the orientation further increases, the direction of principal stress deviates from the grain bedding orientation, resulting in increased smeared cracks and a larger fracturing area, and thus increased compression strength.

4.3.2. *Effect of SOF*

Based on the sensitivity analysis conducted in Section 4.3.1, the specimens with bedding orientations of 0° and 60° exhibit the highest and lowest values of compression strength, respectively, making them the most representative groups. These representative bedding orientations have been selected for sensitivity analysis on the SOF. The generated rock samples with various values of SOF are presented in Fig. 18. Notably, with increasing SOF, the rock samples exhibit a more pronounced layering profile.

The results of compression strength with increasing SOF are shown in Fig. 19. Note that some dispersion still exist due to the variances of the grain structures. As the primary purpose of this section is to understand the evolution laws of compression strength caused by the grain correlation, which have been clearly presented by the existing results. Statistically interpreting the distribution characteristics of compression strength is not the main concern in this study and may require additional simulation results. This aspect will be explored in our future work, drawing inspiration from the research conducted by F. Molina-Gómez, Bulla-Cruz [41]. For the case of 0° bedding orientation, the compression strength exhibits a positive correlation with SOF, whereas it exhibits a negative correlation with SOF for the case of 60°. In addition, when SOF (θ_x) exceeds 100 (normalized by mean grain size), the changes in the grain structure of specimens due to increased SOF becomes insignificant. As a result, the profile of compression strength with increasing SOF gradually reaches a plateau.

To investigate the reason behind the opposite evolution trend of compression strength with increasing SOF, the fracturing patterns of the rock samples with varying bedding orientations and SOFs are shown in Fig. 20. In addition, the proportion of damaged cohesive elements and their failure modes are evaluated and plotted in Fig. 21. Herein, the failure mode includes tension damage and shear damage. A X-shaped fracturing pattern is present in all rock samples for the case of bedding orientation of 0°. As SOF increases, the proportion of damaged cohesive elements increases notably, which is the main reason of the increased compression strength.

Additionally, the proportion of damaged elements due to shearing decreases with increasing SOF, as shown in Fig. 21. This leads to an increase in the amount of tensile cracks and a larger fractured area, as shown in Fig. 20(a). The decrease of damage proportions due to shearing would exhibit a negative impact on the compression strength if the total damage proportion remained the same. However, as the SOF increases, it leads to the development of more tensile cracks and a larger fractured area for the specimens with the grain bedding orientation of 0°, resulting in an increase in the total failure proportion. These findings indicate that the positive effect of increasing the fractured area outweigh the negative effect of the failure mode changes of cohesive elements in such situations, ultimately contributing to the improvement of the compression strength of rock samples with the grain bedding oriented at 0°.

For the rock samples with grain bedding orientation of 60°, the X-shaped fracturing patterns gradually give a way to a narrow shearing band as SOF increases. The proportion of all damaged cohesive elements decreases significantly with the increase of SOF, while the proportion of damaged cohesive elements due to shearing increases, as shown in Fig. 21. Such a phenomenon is consistent with the occurrence of a narrow and concentrated shearing band, as shown in Fig. 20(b). It is thus inferred that the effect of decreasing fractured area would also outweigh the effect of mode changes when the grain bedding correlation is 60°, which leads to the decay of axial compression strengths of the rocks with a correlated grain structure.

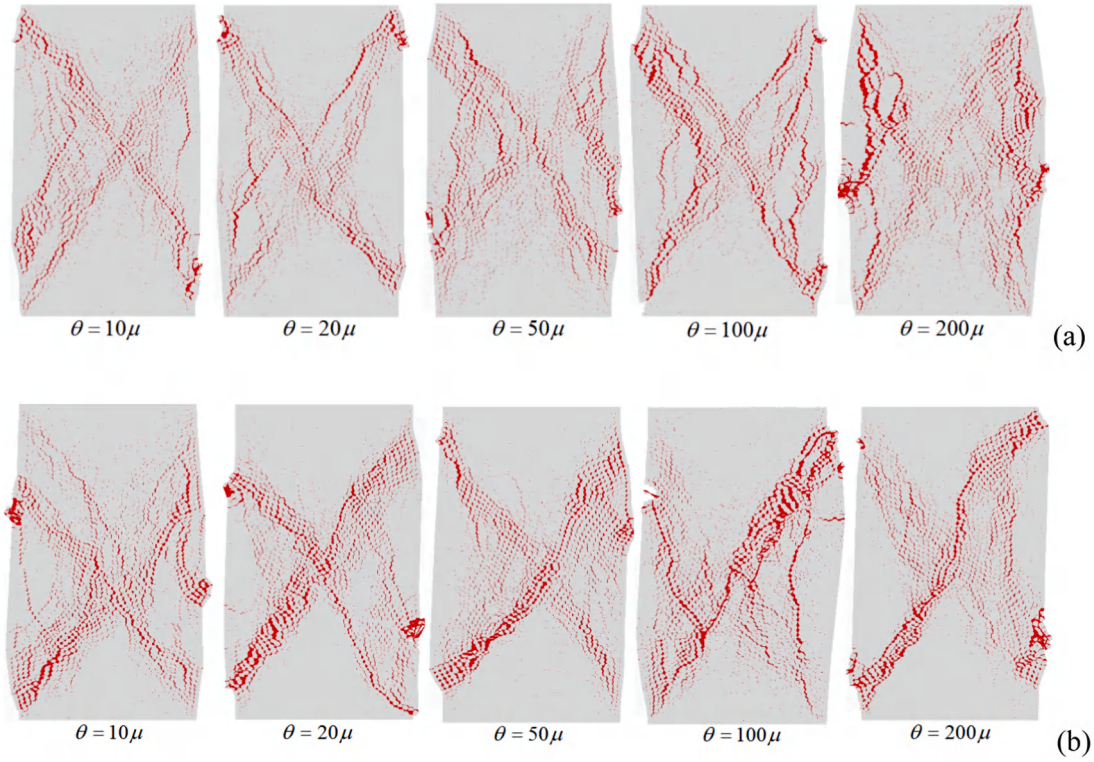

Fig. 20. Fracturing patterns of the rocks with different SOFs (normalized by mean grain size): (a) bedding orientation 0° and (b) bedding orientation 60°.

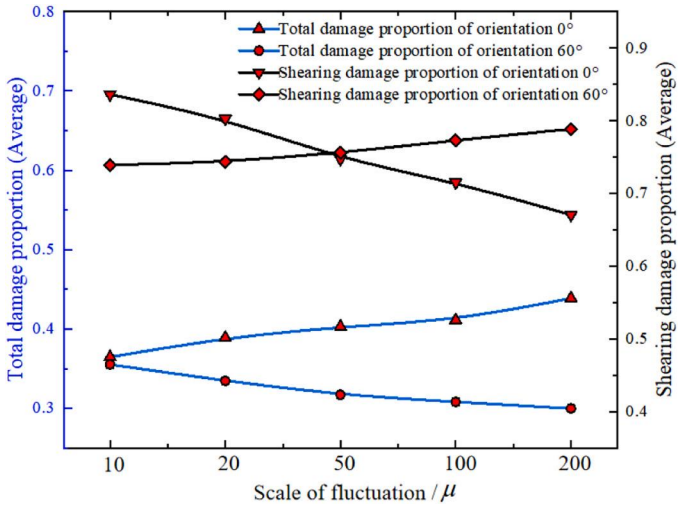

Fig. 21. The damage characteristics of the rocks with different SOFs.

5. Conclusions

In this study, an approach for generating heterogeneous rocks with spatially correlated grain structures is proposed by combining the weighted centroid Voronoi tessellation (WCVT) with random field (RF). Based on the generated rocks with correlated grain structure, the FDEM model is then created by inserting zero-thickness cohesive elements into grain boundaries to model the mechanical behaviors (typically the fracturing behaviour) of the rocks. Numerical examples are presented to demonstrate the effectiveness of RF-WCVT for generating rocks with correlated grain structure and FDEM for modeling heterogeneous rocks. The effects of grain correlation characteristics, in terms of bedding orientations and SOF, on the mechanical and fracturing behavior of heterogeneous rocks are discussed. Some conclusions are as follows:

(1) The proposed RF-WCVT approach provides an effective way to control the grain size distribution and correlation of rocks. The RF statistics of the grain sizes of simulated rocks match well with those of speficied analytical formulations.
(2) The compression strength of heterogeneous rocks decreases as the grain bedding orientation increases from 0° to approximately 60°, whereas it increases as the orientation continues to increase beyond 60°. The highest compression strength is observed at 0° bedding orientation, where many smeared cracks appear. Oppositely, the lowest compression strengths are observed at 60° orientation, where a consistent shearing band is formed.
(3) The compression strength of heterogeneous rocks exhibits distinct evolution trends with SOF for different bedding orientations. For 0° bedding orientation, increasing the SOF leads to an increase in the compression strength, accompanied by increased tensile cracks and fracturing areas. For 60° bedding orientation, the compression strength decreases with SOF. A narrow and concentrated shearing band with increasing shearing failure proportion is observed.

It is anticipated that the proposed RF-WCVT based FDEM approach would become an effective tool for quantifying and predicting the mechanical properties of heterogeneous rocks with spatially correlated and stochastic grain structures. It has the potential to enhance the exploiting and utilization efficiency of various construction and building materials, including porphyritic granite, cemented tailing back-fills and asphalt mixtures. Furthermore, it can also improve the quality and safety of the projects that are constructed on or within these natural or synthetic rock formations.

CRediT authorship contribution statement

Lin Yuexiang: Writing – original draft, Project administration, Methodology, Conceptualization. **Lai Zhengshou:** Writing – review & editing, Validation, Supervision, Methodology. **Ma Jianjun:** Writing –

review & editing, Supervision, Data curation. **Huang Linchong:** Writing – review & editing, Validation, Project administration.

Declaration of Competing Interest

The authors declare that they have no known competing financial interests or personal relationships that could have appeared to influence the work reported in this paper.

Data Availability

Data will be made available on request.

Acknowledgments

The National Natural Science Foundation of China (No. 52208381, 52278422),the Shenzhen Science and Technology Project for Sustainable Development (No. KCXFZ202002011008532), and Programme of Shenzhen Key Laboratory of Green, Efficient and Intelligent Construction of Underground Metro Station. These financial supports are gratefully acknowledged.

References

[1] Q. Chen, A. Seifried, J.E. Andrade, J.W. Baker, Characterization of random fields and their impact on the mechanics of geosystems at multiple scales, Int. J. Numer. Anal. Methods Geomech. 36 (2012) 140–165, https://doi.org/10.1002/nag.999.
[2] S. Cowie, G. Walton, The effect of mineralogical parameters on the mechanical properties of granitic rocks, Eng. Geol. 240 (2018) 204–225, https://doi.org/10.1016/j.enggeo.2018.04.021.
[3] M.W. Davis, Production of conditional simulations via the LU triangular decomposition of the covariance matrix, Math. Geol. 19 (1987) 91–98, https://doi.org/10.1007/BF00898189.
[4] H. Ge, J.C. Quezada, V. Le Houerou, et al., Three-dimensional simulation of asphalt mixture incorporating aggregate size and morphology distribution based on contact dynamics method, Constr. Build. Mater. 302 (2021) 124124, https://doi.org/10.1016/j.conbuildmat.2021.124124.
[5] E. Ghazvinian, M.S. Diederichs, R. Quey, 3D random Voronoi grain-based models for simulation of brittle rock damage and fabric-guided micro-fracturing, J. Rock. Mech. Geotech. Eng. 6 (2014) 506–521, https://doi.org/10.1016/j.jrmge.2014.09.001.
[6] J. Gong, J. Liu, L. Cui, Shear behaviors of granular mixtures of gravel-shaped coarse and spherical fine particles investigated via discrete element method, Powder Technol. 353 (2019) 178–194, https://doi.org/10.1016/j.powtec.2019.05.016.
[7] Y. Gui, H.H. Bui, J. Kodikara, An application of a cohesive fracture model combining compression, tension and shear in soft rocks, Comput. Geotech. 66 (2015) 142–157, https://doi.org/10.1016/j.compgeo.2015.01.018.
[8] Y.L. Gui, Z.Y. Zhao, C. Zhang, S.Q. Ma, Numerical investigation of the opening effect on the mechanical behaviours in rocks under uniaxial loading using hybrid continuum-discrete element method, Comput. Geotech. 90 (2017) 55–72, https://doi.org/10.1016/j.compgeo.2017.05.021.
[9] Y.L. Gui, Z.Y. Zhao, J. Kodikara, H.H. Bui, S.Q. Yang, Numerical modelling of laboratory soil desiccation cracking using UDEC with a mix-mode cohesive fracture model, Eng. Geol. 202 (2016) 14–23, https://doi.org/10.1016/j.enggeo.2015.12.028.
[10] N. Güneş Yılmaz, R. Mete Goktan, Y. Kibici, Relations between some quantitative petrographic characteristics and mechanical strength properties of granitic building stones, Int. J. Rock. Mech. Min. Sci. 48 (2011) 506–513, https://doi.org/10.1016/j.ijrmms.2010.09.003.
[11] J. Guo, B. Luo, C. Lu, J. Lai, J. Ren, Numerical investigation of hydraulic fracture propagation in a layered reservoir using the cohesive zone method, Eng. Fract. Mech. 186 (2017) 195–207, https://doi.org/10.1016/j.engfracmech.2017.10.013.
[12] X., J. Hao, X., T. Feng, C., X. Yang, Q. Jiang, Analysis of EDZ Development of Columnar Jointed Rock Mass in the Baihetan Diversion Tunnel, Rock. Mech. Rock. Eng. 49 (2016) 1289–1312, https://doi.or/10.1007/s00603-015-0829-4.
[13] L. Huang, S. Huang, Z. Lai, On the optimization of site investigation programs using centroidal Voronoi tessellation and random field theory, Comput. Geotech. 118 (2020) 103331, https://doi.org/10.1016/j.compgeo.2019.103331.
[14] L.C. Huang, J.J. Ma, M.F. Lei, et al., Soil-water inrush induced shield tunnel lining damage and its stabilization: a case study, Tunnelling and Underground Space Technology 97 (2020) 103290, https://doi.org/10.1016/j.tust.2020.103290.
[15] J.G. James, Basalt columns: large scale constitutional supercooling? J. Volcano Geotherm. Res 184 (2009) 347–350, https://doi.org/10.1016/j.jvolgeores.2009.04.017.
[16] R. Jamshidi Chenari, H. Kamyab Farahbakhsh, Generating non-stationary random fields of auto-correlated, normally distributed CPT profile by matrix decomposition method, Georisk: Assess. Manag. Risk Eng. Syst. Geohazards 9 (2015) 96–108, https://doi.org/10.1080/17499518.2015.1033429.
[17] H.Z. Jiao, Q. Zhang, Y.X. Yang, T.Y. Yang, Effect of interface roughness on mechanical properties of layered cemented tailings backfill, Constr. Build. Mater. 409 (2023) 134071, https://doi.org/10.1016/j.conbuildmat.2023.134071.
[18] T. Kazerani, J. Zhao, Micromechanical parameters in bonded particle method for modelling of brittle material failure, Int. J. Numer. Anal. Methods Geomech. 34 (2010) 1877–1895, https://doi.org/10.1002/nag.884.
[19] Z. Lai, Q. Chen, L. Huang, Evaluating the hydromechanical responses of seabed–pipelines with rotated anisotropic heterogeneous seabed properties, Ocean Eng. 234 (2021) 109226, https://doi.org/10.1016/j.oceaneng.2021.109226.
[20] Z.S. Lai, S.W. Zhao, J.D. Zhao, et al., Signed distance field framework for unified DEM modeling of granular media with arbitrary particle shapes, Comput. Mech. 70 (4) (2022) 763–783, https://doi.org/10.1007/s00466-022-02220-8.
[21] D.-Q. Li, S.-H. Jiang, Z.-J. Cao, W. Zhou, C.-B. Zhou, L.-M. Zhang, A multiple response-surface method for slope reliability analysis considering spatial variability of soil properties, Eng. Geol. 187 (2015) 60–72, https://doi.org/10.1016/j.enggeo.2014.12.003.
[22] H. Li, J. Yang, Y. Han, C. Yang, J.J.K. Daemen, P. Li, Weibull grain-based model (W-GBM) for simulating heterogeneous mechanical characteristics of salt rock, Eng. Anal. Bound. Elem. 108 (2019) 227–243, https://doi.org/10.1016/j.enganabound.2019.09.001.
[23] M. Li, P. Guo, D. Stolle, L. Liang, Modeling method for a rock matrix with inclusions distributed and hydraulic fracturing characteristics, J. Pet. Sci. Eng. 157 (2017) 409–421, https://doi.org/10.1016/j.petrol.2017.07.017.
[24] M. Li, P. Guo, D. Stolle, S. Sun, L. Liang, Modeling hydraulic fracture propagation in a saturated porous rock media based on EPHF method, J. Nat. Gas. Sci. Eng. 89 (2021) 103887, https://doi.org/10.1016/j.jngse.2021.103887.
[25] X.F. Li, H.B. Li, J. Zhao, 3D polycrystalline discrete element method (3PDEM) for simulation of crack initiation and propagation in granular rock, Comput. Geotech. 90 (2017) 96–112, https://doi.org/10.1016/j.compgeo.2017.05.023.
[26] X.Y. Li, L.M. Zhang, J.H. Li, Using conditioned random field to characterize the variability of geologic profiles, J. Geotech. Geoenviron. Eng. 142 (2016) 04015096, https://doi.org/10.1061/(ASCE)GT.1943-5606.0001428.
[27] Y. Lin, X. Wang, J. Ma, L. Huang, A systematic framework for the 3D finite-discrete modelling of binary mixtures considering irregular block shapes and cohesive block-matrix interfaces, Powder Technol. 398 (2022) 117070, https://doi.org/10.1016/j.powtec.2021.117070.
[28] Y. Lin, X. Wang, J. Ma, L. Huang, A finite-discrete element based appoach for modelling the hydraulic fracturing of rocks with irregular inclusions, Eng. Fract. Mech. 261 (2022) 108209, https://doi.org/10.1016/j.engfracmech.2021.108209.
[29] Y. Lin, Z.-Y. Yin, X. Wang, L. Huang, A systematic 3D simulation method for geomaterials with block inclusions from image recognition to fracturing modelling, Theor. Appl. Fract. Mech. 117 (2022) 103194, https://doi.org/10.1016/j.tafmec.2021.103194.
[30] Y. Lin, C. Li, J. Ma, M. Lei, L. Huang, Effects of void morphology on fracturing characteristics of porous rock through a finite-discrete element method, J. Nat. Gas. Sci. Eng. 104 (2022) 104684, https://doi.org/10.1016/j.jngse.2022.104684.
[31] Y. Lin, J. Ma, Z. Lai, L. Huang, M. Lei, A FDEM approach to study mechanical and fracturing responses of geo-materials with high inclusion contents using a novel reconstruction strategy, Eng. Fract. Mech. 282 (2023) 109171, https://doi.org/10.1016/j.engfracmech.2023.109171.
[32] A. Lisjak, B.S.A. Tatone, G. Grasselli, T. Vietor, Numerical modelling of the anisotropic mechanical behaviour of opalinus clay at the laboratory-scale using FEM/DEM, Rock. Mech. Rock. Eng. 47 (2014) 187–206, https://doi.org/10.1007/s00603-012-0354-7.
[33] Q. Liu, Y. Jiang, Z. Wu, J. He, A Voronoi element based-numerical manifold method (VE-NMM) for investigating micro/macro-mechanical properties of intact rocks, Eng. Fract. Mech. 199 (2018) 71–85, https://doi.org/10.1016/j.engfracmech.2018.05.010.
[34] Q. Liu, Y. Jiang, Z. Wu, Z. Qian, X. Xu, Numerical modeling of acoustic emission during rock failure process using a Voronoi element based – explicit numerical manifold method, Tunn. Undergr. Space Technol. 79 (2018) 175–189, https://doi.org/10.1016/j.tust.2018.05.009.
[35] M.K. Lo, Y.F. Leung, Probabilistic analyses of slopes and footings with spatially variable soils considering cross-correlation and conditioned random field, J. Geotech. Geoenviron. Eng. 143 (2017) 04017044, https://doi.org/10.1061/(ASCE)GT.1943-5606.0001720.
[36] W., B. Lu, Z., D. Zhu, Y., X. He, X., C. Que, Strength characteristics and failure mechanism of a columnar jointed rock mass under uniaxial, triaxial, and true triaxial confnement, Rock. Mech. Rock. Eng. 54 (2021) 2425–2439, https://doi.org/10.1007/s00603-021-02400-7.
[37] J. Ma, J. Chen, J. Guan, Y. Lin, W. Chen, L. Huang, Implementation of Johnson-Holmquist-Beissel model in four-dimensional lattice spring model and its application in projectile penetration, Int. J. Impact Eng. 170 (2022) 104340, https://doi.org/10.1016/j.ijimpeng.2022.104340.
[38] Ma J.J., Ding W.J., Lin Y.X., et al., A fast and efficient particle packing generation algorithm with controllable gradation for discontinuous deformation analysis. Geomechanics and Geophysics for Geo-Energy and Geo-Resources, 9(1): 1–27. https://doi.org/10.1007/s40948–023-00637-w.
[39] J.J. Ma, J.X. Zhao, Y.X. Lin, et al., Study on tamped spherical detonation-induced dynamic responses of rock and PMMA through mini-chemical explosion tests and a four-dimensional lattice spring model, Comput. Geotech., Rock. Mech. Rock. Eng. 56 (10) (2023) 7357–7375, https://doi.org/10.1007/s00603-023-03426-9.
[40] Q.-X. Meng, H.-L. Wang, W.-Y. Xu, Y.-L. Chen, Numerical homogenization study on the effects of columnar jointed structure on the mechanical properties of rock mass, Int. J. Rock. Mech. Min. Sci. 124 (2019) 104127, https://doi.org/10.1016/j.ijrmms.2019.104127.

[41] F. Molina-Gómez, L.A. Bulla-Cruz, A novel approach for the control of grain size distributions based on variance analysis, Constr. Build. Mater. 285 (2021) 122748, https://doi.org/10.1016/j.conbuildmat.2021.122748.
[42] A.S. Mreyen, D. Donati, D. Elmo, F.V. Donze, Dynamic numerical modelling of co-seismic landslides using the 3D distinct element method: Insights from the Balta rockslide (Romania), Eng. Geol. (2022) 106774, https://doi.org/10.1016/j.enggeo.2022.106774.
[43] H. Niandou, J.F. Shao, J.P. Henry, D. Fourmaintraux, Laboratory investigation of the mechanical behaviour of Tournemire shale, Int. J. Rock. Mech. Min. Sci. 34 (1997) 3–16, https://doi.org/10.1016/S1365-1609(97)80029-9.
[44] D.O. Potyondy, P.A. Cundall, A bonded-particle model for rock, Int. J. Rock. Mech. Min. Sci. 41 (8) (2004) 1329–1364.
[45] X., C. Que, Z., D. Zhu, L., M. Zhou, Z., H. Niu, H., N. Huang, Strength and failure characteristics of an irregular columnar jointed rock mass under polyaxial stress conditions, Rock. Mech. Rock. Eng. 55 (2022) 7223–7242, https://doi.org/10.1007/s00603-022-03023-2.
[46] S. Sbi, W. Borja, S. Mansouri, et al., An advance understanding of the alkali activation of cover layers waste rocks from phosphate mines: mechanical, structure and microstructure studies, Constr. Build. Mater. 346 (2022) 128472, https://doi.org/10.1016/j.conbuildmat.2022.128472.
[47] B.S.A. Tatone, G. Grasselli, A calibration procedure for two-dimensional laboratory-scale hybrid finite–discrete element simulations, Int. J. Rock. Mech. Min. Sci. 75 (2015) 56–72, https://doi.org/10.1016/j.ijrmms.2015.01.011.
[48] A. Turon, P.P. Camanho, J. Costa, C.G. Dávila, A damage model for the simulation of delamination in advanced composites under variable-mode loading, Mech. Mater. 38 (2006) 1072–1089, https://doi.org/10.1016/j.mechmat.2005.10.003.
[49] H.L. Wang, Z.Y. Yin, P. Zhang, Y.F. Jin, Straightforward prediction for air-entry value of compacted soils using machine learning algorithms, Eng. Geol. 279 (2020) 105911, https://doi.org/10.1016/j.enggeo.2020.105911.
[50] J. Wang, J.X. Fu, W.D. Song, Mechanical properties and microstructure of layered cemented paste backfill under triaxial cyclic loading and unloading, Constr. Build. Mater. 257 (2020) 119540, https://doi.org/10.1016/j.conbuildmat.2020.119540.
[51] Z. Wang, C. Shi., H. Chen, M.. Lei, Probabilistic evaluation for excavation-induced longitudinal responses of existing shield tunnel in spatially random soils, Computers and Geotechnics (2024) 106110, https://doi.org/10.1016/j.compgeo.2024.106110.
[52] Z. Wang, C. Shi, H. Chen, Z. Peng, Y. Sun, X.. Zheng, Probabilistic analysis of the longitudinal performance of shield tunnels based on a simplified finite element procedure and its surrogate model considering spatial soil variability, Computers and Geotechnics 162 (2023) 105662, https://doi.org/10.1016/j.compgeo.2023.105662.
[53] H.-R. Wenk, J. Huang, M. Devoe, J.G. omez-Barreiro, R. Vasin, Y. Ren, Crystallographic and shape preferred orientation producing anisotropy in slates from Northern Spain, J. Struct. Geol. 164 (2022) 104730, https://doi.org/10.1016/j.jsg.2022.104730.
[54] Z. Wu, L. Ma, L. Fan, Investigation of the characteristics of rock fracture process zone using coupled FEM/DEM method, Eng. Fract. Mech. 200 (2018) 355–374, https://doi.org/10.1016/j.engfracmech.2018.08.015.
[55] Z. Wu, X. Xu, Q. Liu, Y. Yang, A zero-thickness cohesive element-based numerical manifold method for rock mechanical behavior with micro-Voronoi grains, Eng. Anal. Bound. Elem. 96 (2018) 94–108, https://doi.org/10.1016/j.enganabound.2018.08.005.
[56] Z. Wu, F. Yu, P. Zhang, X. Liu, Micro-mechanism study on rock breaking behavior under water jet impact using coupled SPH-FEM/DEM method with Voronoi grains, Eng. Anal. Bound. Elem. 108 (2019) 472–483, https://doi.org/10.1016/j.enganabound.2019.08.026.
[57] W., M. Xiao, R., G. Deng, Z., B. Zhong, X., M. Fu, C., Y. Wang, Experimental study on the mechanical properties of simulated columnar jointed rock masses, J. Geophys Eng. 12 (1) (2015) 80–89, https://doi.org/10.1088/1742-2132/12/1/80.
[58] C. Yan, H. Guo, Z. Tang, Three-dimensional continuous-discrete pore-fracture mixed seepage model and hydro-mechanical coupling model to simulate hydraulic fracturing, J. Pet. Sci. Eng. 215 (2022) 110510, https://doi.org/10.1016/j.petrol.2022.110510.
[59] C. Yan, Y. Zheng, D. Huang, G. Wang, A coupled contact heat transfer and thermal cracking model for discontinuous and granular media, Comput. Methods Appl. Mech. Eng. 375 (2021) 113587, https://doi.org/10.1016/j.cma.2020.113587.
[60] C. Yao, Q.H. Jiang, J.F. Shao, C.B. Zhou, A discrete approach for modeling damage and failure in anisotropic cohesive brittle materials, Eng. Fract. Mech. 155 (2016) 102–118, https://doi.org/10.1016/j.engfracmech.2016.01.012.
[61] Y.L. Yaphary, Z. Leng, H. Wang, et al., Characterization of nanoscale cracking at the interface between virgin and aged asphalt binders based on molecular dynamics simulations, Constr. Build. Mater. 335 (2022) 127475, https://doi.org/10.1016/j.conbuildmat.2022.127475.
[62] P. Yin, C. Zhao, J. Ma, C. Yan, L. Huang, Experimental study of non-linear fluid flow though rough fracture based on fractal theory and 3D printing technique, Int. J. Rock. Mech. Min. Sci. 129 (2020) 104293, https://doi.org/10.1016/j.ijrmms.2020.104293.
[63] L. Zhai, H. Zhang, D. Pan, Y. Zhu, J. Zhu, Y. Zhang, C. Chen, Optimisation of hydraulic fracturing parameters based on cohesive zone method in oil shale reservoir with random distribution of weak planes, J. Nat. Gas. Sci. Eng. 75 (2020) 103130, https://doi.org/10.1016/j.jngse.2019.103130.
[64] P. Zhang, L. Jin, X. Du, D. Lu, Computational homogenization for mechanical properties of sand cobble stratum based on fractal theory, Eng. Geol. 232 (2018) 82–93, https://doi.org/10.1016/j.enggeo.2017.11.013.
[65] B. Zhou, D. Wei, Q. Ku, et al., Study on the effect of particle morphology on single particle breakage using a combined finite-discrete element method, Comput. Geotech. 122 (2020). DOI:10.1016/j.compgeo.2020.103532.
[66] J. Zhou, H. Lan, L. Zhang, D. Yang, J. Song, S. Wang, Novel grain-based model for simulation of brittle failure of Alxa porphyritic granite, Eng. Geol. 251 (2019) 100–114, https://doi.org/10.1016/j.enggeo.2019.02.005.
[67] X.Y. Zhuang, S.W. Zhou, M. Sheng, G.S. Li, On the hydraulic fracturing in naturally-layered porous media using the phase field method, Eng. Geol. 266 (2020) 105306, https://doi.org/10.1016/j.enggeo.2019.105306.